JACS
JOURNAL OF THE AMERICAN CHEMICAL SOCIETY
Article
pubs.acs.org/JACS

Förster Energy Transport in Metal–Organic Frameworks Is Beyond Step-by-Step Hopping

Qiongqiong Zhang,[†,§] Cankun Zhang,[†,§] Lingyun Cao,[†,§] Zi Wang,[†] Bing An,[†] Zekai Lin,[‡] Ruiyun Huang,[†] Zhiming Zhang,[†,∥] Cheng Wang,*[,†] and Wenbin Lin*[,†,‡]

[†]Collaborative Innovation Center of Chemistry for Energy Materials, State Key Laboratory of Physical Chemistry of Solid Surfaces, Department of Chemistry, College of Chemistry and Chemical Engineering, Xiamen University, Xiamen 361005, PR China

[‡]Department of Chemistry, University of Chicago, 929 E 57th Street, Chicago, Illinois 60637, United States

Supporting Information

ABSTRACT: Metal–organic frameworks (MOFs) with light-harvesting building blocks designed to mimic photosynthetic chromophore arrays in green plants provide an excellent platform to study exciton transport in networks with well-defined structures. A step-by-step exciton random hopping model made of the elementary steps of energy transfer between only the nearest neighbors is usually used to describe the transport dynamics. Although such a nearest neighbor approximation is valid in describing the energy transfer of triplet states via the Dexter mechanism, we found it inadequate in evaluating singlet exciton migration that occurs through the Förster mechanism, which involves one-step jumping over longer distance. We measured migration rates of singlet excitons on two MOFs constructed from truxene-derived ligands and zinc nodes, by monitoring energy transfer from the MOF skeleton to a coumarin probe in the MOF cavity. The diffusivities of the excitons on the frameworks were determined to be 1.8×10^{-2} cm^2/s and 2.3×10^{-2} cm^2/s, corresponding to migration distances of 43 and 48 nm within their lifetimes, respectively. "Through space" energy-jumping beyond nearest neighbor accounts for up to 67% of the energy transfer rates. This finding presents a new perspective in the design and understanding of highly efficient energy transport networks for singlet excited states.

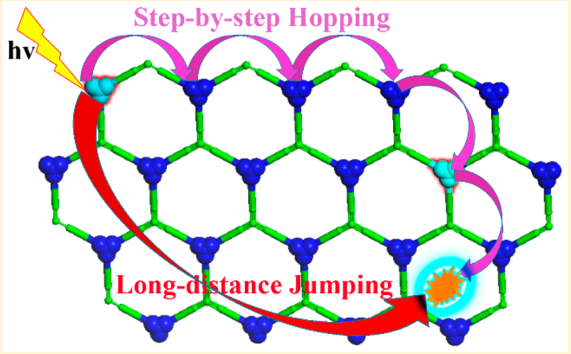

INTRODUCTION

Natural photosynthesis begins by efficiently funneling energy collected from sunlight to reaction centers via exciton transport.[1,2] To study this process, exciton migrations over long distances have been explored in artificial networks[3−15] such as light-harvesting metal–organic frameworks (MOFs).[16−20] As a structurally well-defined platform,[21−24] MOFs not only present new opportunities for the judicious design of antenna materials using chromophore-based ligands,[25−36] but also enable study of energy transport dynamics in networks with well-defined structures.[37−46] The chromophores can be isolated from each other on the MOF skeleton with interchromophore distances of usually 1−2 nm, a value very close to that in natural photosynthetic membranes (e.g., interchlorophyll distances are 1−1.3 nm in chloroplasts).[47−49] This ligand separation in space leads to energy transfer in a weak electronic coupling regime, in contrast to molecular crystals with direct close packing and strong electronic coupling. MOF crystals are thus extremely favorable crystalline models for photosynthetic antenna arrays in green plants and photosynthetic bacteria.[50,51]

Exciton dynamics on MOF networks have been described as a step-by-step random hopping, which comprises elementary steps of energy transfer between adjacent ligands.[37,40] We adopted this understanding of nearest-neighbor hopping (NNH) in our previous studies on efficient energy transport of triplet-states in a series of MOFs containing $Ru(bpy)_3^{2+}$ and $Os(bpy)_3^{2+}$.[41,52] The nearest-neighbor approximation was confirmed by the short energy transfer distance of triplet ^{3}MLCT states mainly via the Dexter mechanism, which requires wave function overlap between the donor and the acceptor. This simple successive hopping model also describes singlet exciton dynamics in porphyrin-based MOFs.[40] However, the model cannot fully describe Förster-type singlet exciton dynamics due to the involvement of the "through-space" jumping beyond nearest neighbors. Recent reports of Förster energy transfer between dopants in single steps over long distances in MOFs suggest the importance of including jumping beyond nearest neighbors (JBNN, Figure 1).[45,46]

In this work, we studied Förster energy transport of singlet excitons in two light-harvesting MOFs with truxene-based ligands. We found that the step-by-step NNH model was inadequate for quantifying our experimental observations because JBNN accounted for up to 67% of migration rates in our systems.

Received: February 5, 2016
Published: March 25, 2016

DOI: 10.1021/jacs.6b01345
J. Am. Chem. Soc. 2016, 138, 5308−5315

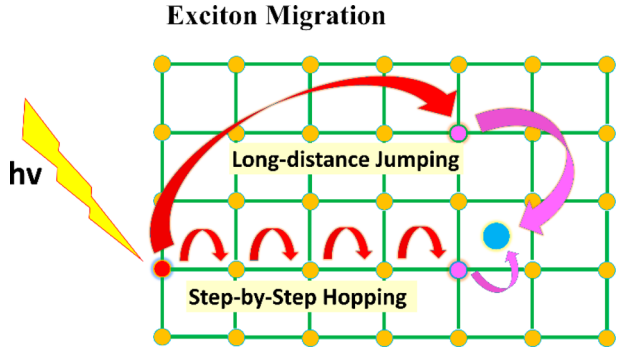

Figure 1. Cartoon showing two distinct pathways in exciton migration on a network of chromophores: (1) Step-by-step nearest neighbor hopping (NNH); (2) Long-distance jumping. The exciton can diffuse on the network and get transferred to acceptor molecules (e.g., reaction centers in photosynthesis) jumping beyond nearest neighbors (JBNN) in the network.

Exciton migration was monitored by employing coumarin dye molecules in the MOF cavity as an emissive observer.[6] Excitons move around the MOF skeleton via ligand-to-ligand energy exchange until they find a coumarin, after which the energy is transferred to the dye. The more mobile the exciton, the greater the likelihood it will end up on a dye molecule within its emission lifetime. Truxene ligands correspond to the antenna array for light-harvesting in natural photosynthetic systems, and coumarin dyes correspond to reaction centers that accept the excitons. The emission ratio between the coumarin dye and the ligands thus serves as a sensitive measurement of exciton migration rates. We found the exciton diffusivities on the two MOF skeletons to be 1.8×10^{-2} cm^2/s and 2.3×10^{-2} cm^2/s, which correspond to migration distances of 43 and 48 nm within their lifetimes, respectively.

RESULTS AND DISCUSSION

MOF Synthesis and Structural Characterization. The two MOFs in our study (truMOF-1 and truMOF-2) were constructed from truxene-tribenzoate ligands (5,5′,10,10′,15,15′-hexaethyltruxene-2,7,12-tribenzoic acid = H_3**L**, see Scheme S1 and Figure S1−S3 in Supporting Information [SI]) and $Zn_{10}(\mu_4\text{-O})_4(\text{carboxylate})_{12}$ or $Zn_4(\mu_4\text{-O})(OH)_3(OH_2)_3(\text{carboxylate})_3$ secondary building units (SBUs) as shown in Figure 2. Their structures were determined by single crystal X-ray diffraction studies (see Table S1, S2; see Figure S4, S5 for powder X-ray diffraction patterns and Figure S6−S9 for chemical composition determination). Both MOFs crystallize in the cubic crystal system, with the space group of $F\bar{4}3m$ for truMOF-1 and $I2_13$ for truMOF-2. In truMOF-1, four of the triangular **L** ligands form a tetrahedral cage and the cages are further linked to each other on the vertex through the SBUs to give a net of *ttt* topology and a framework formula of $Zn_{10}(\mu_4\text{-O})_4(\mathbf{L})_4$. The center-to-center distance between adjacent ligands in the same cage is 0.87 nm, while distances between cages are larger with the shortest ligand-to-ligand distance of 1.8 nm. In truMOF-2, the **L** ligands with the C_{3h} symmetry and the 3-connected SBUs link to each other alternately to give 2-fold interpenetrated 3,3-connected nets of *srs* topology and a framework formula of $Zn_4(\mu_4\text{-O})(OH)_3(OH_2)_3(\mathbf{L})$. Each ligand has three nearest neighbors on the interpenetrated net with a ligand-to-ligand distance of 1.3 nm. Both MOFs possess 3D-connected channels with pore sizes of 2.2 nm for truMOF-1 and 1.7 nm for truMOF-2. The high cubic symmetry of the crystals together with the random orientations of transition dipoles due to the C_{3h} symmetry of the ligands lead to macroscopically isotropic exciton transport dynamics without the usual complication from crystal anisotropy.

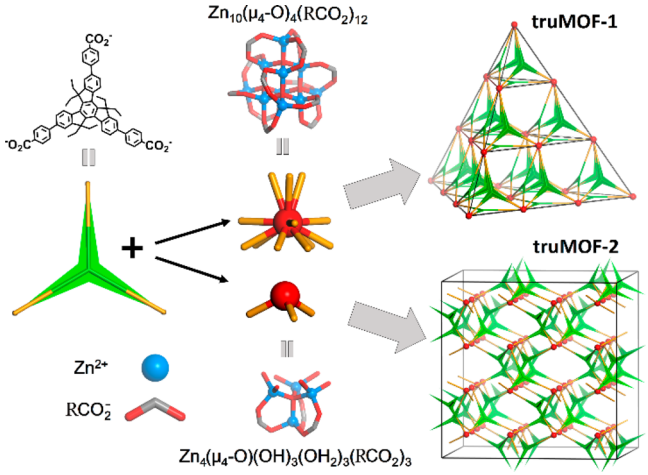

Figure 2. Structures of truMOF-1 and truMOF-2. The green triblade represents the truxene ligand with C_{3h} symmetry and the red dots represent the Zn_{10} and Zn_4 SBUs in truMOF-1 and -2, respectively.

Dye Loading. Coumarin dye molecules were loaded into the porous MOFs by a solution impregnation method. The crystals were equilibrated with EtOH solutions of coumarin 343 for 48 h, followed by briefly washing away the dye molecules on the external surface of the crystal with fresh solvent. The dye loading percentage was quantified by combined fluorescence and UV−vis measurements of digested DMF solution of dye@MOF hybrids, and can be fine-tuned by using coumarin solutions of different dye concentrations for loading (see Figure S10−S18). The dye loading level expressed as coumarin dye/MOF ligand ratio ranges from 0% to 2.1% in the experiments. These doping levels are close to the ratio (0.45−5%) between reaction centers and light-harvesting chlorophylls in the photosynthetic system of green plants.[47,53−55]

The positions of adsorbed dye molecules were estimated from molecular dynamic calculations (see the following sections). The dye configurations with lowest energies were plotted in Figure S19. The coumarin dye molecule in truMOF-1 adheres to one of the benzene rings of a truxene ligand, and sits in the valley formed by two adjacent truxene ligands and the SBU. In truMOF-2, the dye molecule is in close contact with three adjacent truxene ligands and sits in a bowl formed by the three ligands.

Fluorescence Measurement and Energy Transfer Efficiency. The overlap of the coumarin absorption and ligand **L** emission spectra as shown in Figure 3 suggests possible efficient energy transfer from the ligand to the dye. The steady state emissions of the dye@MOFs confirmed such transfer. Upon excitation at the ligand absorption wavelength of 370 nm,[56] two emission peaks appeared in the spectra, corresponding to the emission of the **L** ligand (λ_{max} = 395 nm) and the emission of dye resulting from energy transfer (λ_{max} = 485 nm). This energy transfer can also be verified by the excitation spectra monitored at the dye emission maximum at 485 nm, which showed two excitation peaks corresponding to direct excitation of the dye (λ_{max}= 445 nm) and excitation of the ligand (λ_{max}= 370 nm) followed by energy transfer to the dye

DOI: 10.1021/jacs.6b01345
J. Am. Chem. Soc. 2016, 138, 5308−5315

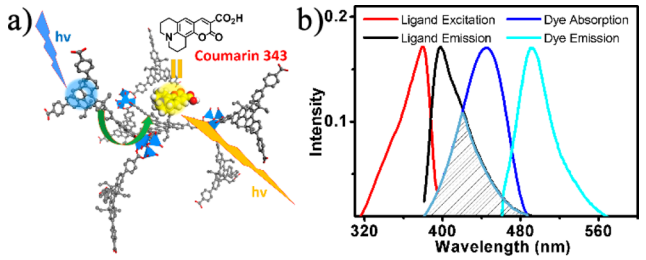

Figure 3. (a) Scheme showing the energy transfer from the truxene ligand on the MOF to the coumarin dye. (b) Excitation/absorption and emission spectra of the ligand in MOF and the dye molecule in DMF.

(Figure 4a). All the fluorescence measurements in this work were performed at room temperature.

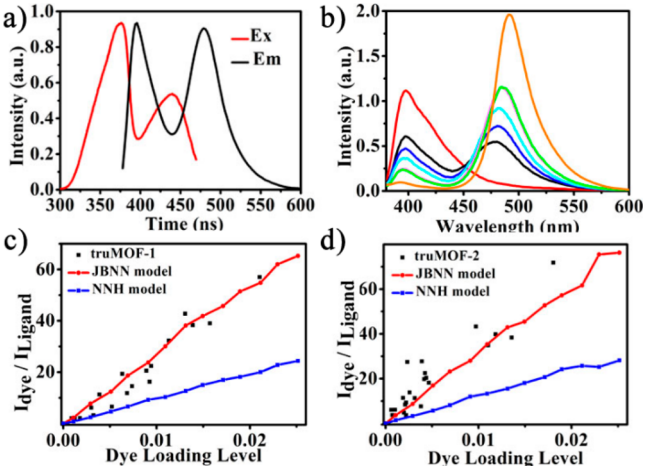

Figure 4. (a) Emission spectra of dye@truMOF-1 with excitation at 370 nm and excitation spectra of dye@truMOF-1 monitored at the emission wavelength of 485 nm. (b) Emission spectra of dye@truMOF-2 with excitation at 370 nm, with dye loading levels of 0% (red), 0.12% (black), 0.32% (blue), 0.52% (cyan), 0.74% (pink), 0.93% (green), 1.57% (orange). (c) I_{dye}/I_{ligand} of truMOF-1 as a function of dye loading level, together with simulated values from the NNH model and the model including JBNN. (d) I_{dye}/I_{ligand} of dye@truMOF-2 as a function of dye loading level, together with simulated values from the NNH model and the model including JBNN.

We systematically changed the excitation wavelength to collect emission spectra and assembled them into the 2D map shown in Figure 5. On the map, the vertical axis represents the excitation wavelength and the horizontal axis represents the emission wavelength. The energy transfer is easily identified on the 2D map as a "cross-peak" (λ_{ex} = 370 nm; λ_{em} = 485 nm) between the two peaks associated with ligand ex/em (λ_{ex} = 370 nm ; λ_{em} = 395 nm) and dye ex/em (λ_{ex} = 445 nm; λ_{em} = 485 nm), as a result of exciting at the ligand wavelength but emitting at the dye wavelength due to energy transfer.

This energy transfer peak becomes more visible as higher amounts of coumarin dye were loaded into the MOFs (Figure 4b). As the dye concentration increases to 0.98%, the truxene ex/em peak almost disappears, corresponding to close to unity energy transfer efficiency. The ratios between the integrated intensities of the dye and the ligand (I_{dye}/I_{ligand}) at the excitation wavelength of ligand absorption serve as a figure of merit to evaluate the degree of energy transfer (Figure 4c,d). These data, together with the simulated values from different

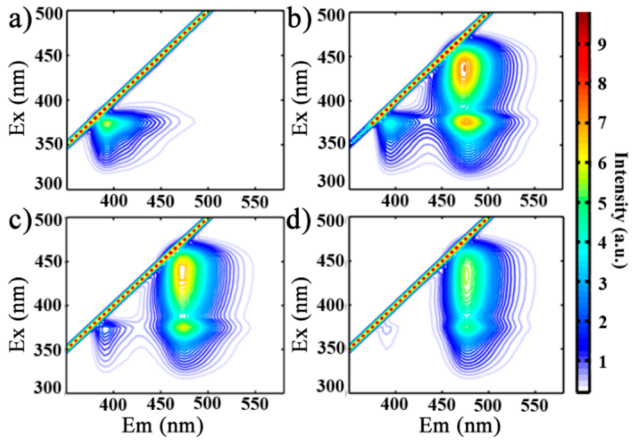

Figure 5. 2D fluorescence spectra of the dye@truMOF-1 assembly at different dye loading levels: (a) 0%, (b) 0.24%, (c) 0.42%, (d) 0.98%.

models, suggest significant contribution of exciton jumping beyond nearest neighbors (see the following sections). An I_{dye}/I_{ligand} value as high as 57 was obtained for truMOF-1 with a dye loading level of 2.1%, corresponding to energy transfer efficiency of 98% as calculated by

$$\text{efficiency} = \frac{I_{dye}/I_{ligand}}{\frac{I_{dye}}{I_{ligand}} + QY_{dye}/QY_{ligand}}$$

where QY stands for quantum yield (Figure S20, S21). TruMOF-2 shows even more efficient energy transfer with an I_{dye}/I_{ligand} value of 72 at a dye loading level of 1.8%.

Time-Resolved Emission Measurements and Exciton Migration. Time-resolved emission measurements were used to delineate the underlying dynamics of exciton migration and energy transfer. The intensities of the time-resolved emission for the ligand and the dye are proportional to their excited state populations as a function of time, and can be obtained after deconvolution of the excitation pulse from the recorded curves (Figure 6, Figure S22, S23 and Table S3). Even for the very short lifetime of the ligand during energy transfer, a confident result with signal/noise >5 can be obtained. The coumarin emission rises in the beginning with the decrease of the ligand emission on the time scale of ligand lifetime, and then goes back to ground state by emissive transition and nonemissive

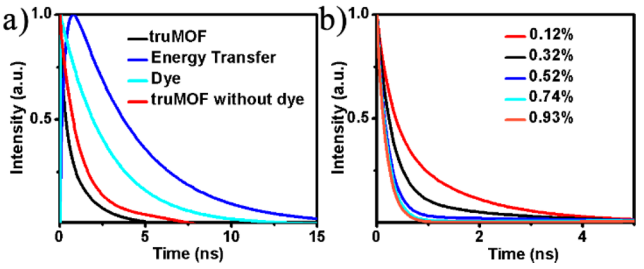

Figure 6. (a) Time-resolved emission traces of dye@truMOF-1 with a dye loading level of 0.12% [truMOF (black): ex@339 nm em@385 nm; Energy Transfer (blue): ex@375 nm, em@485 nm; Dye-(cyan):ex@455 nm, em@495 nm] and control sample of truMOF-1 without dye (red): ex@339 nm em@400 nm. Noise has been removed in the deconvolution routine. (b) Time-resolved emission traces of truMOF-1 with different dye doping levels (excited at 375 nm and detected at 485 nm).

DOI: 10.1021/jacs.6b01345
J. Am. Chem. Soc. 2016, 138, 5308−5315

relaxation at the dye lifetime. The existence of this initial growth period again confirms the energy transfer from the ligand to the dye.

The shortened emission lifetime of the ligand after dye loading is consistent with a diffusional quenching mechanism for the ligand-to-dye energy transfer, as compared to static quenching. The major difference between these two quenching modes is that the relative distance between the emitter and the quencher changes in the diffusional quenching on the time scale of the excited state lifetime, while this distance does not change in static quenching. In the dye@MOF hybrid, the physical distance between the ligand (emitter) and the dye (quencher) does not change on the time scale of ligand lifetime, but the excited state can migrate on the framework through multiple ligand-to-ligand energy transfer. This exciton migration changes the relative distance between the excited state and the dye acceptor, thus effectively creating conditions for diffusional quenching that leads to the same mathematical consequences as molecular diffusion. The exciton migration greatly enhances the energy transfer efficiency and is widely used by light-harvesting systems in natural photosynthesis, as well as in artificial systems for amplified quenching-based fluorescent detection.[10]

Simulation of Exciton Dynamics. The above measurements and analyses showed that energy transfer in truMOF-2 is more efficient than that in truMOF-1. As the two MOFs were constructed from the same ligands and the same metal ions, the difference must result from their structures. To understand the relationship between structure and energy transfer and develop a principle for designing light-harvesting materials, we performed simulations of exciton dynamics in these systems.

The rate of energy transfer for singlet excitons can be described by the Förster energy transfer theory (but beyond the point-dipole approximation, see below).[40,57−59] With crystal structures, energy transfer rates were obtained between every two ligands in a 7 × 7 × 7 cube containing 343 unit-cells and 5488 **L** ligands for truMOF-1, or 2744 **L** ligands for truMOF-2.

We first used the nearest neighbor approximation, considering exciton hopping only between ligands with a center-to-center distance of less than 2.0 nm (nearest neighbors). The simulations, however, significantly underestimated the energy transfer efficiency of truMOF-1 compared to the experimental results. After adding back the energy transfer over longer distances, reasonable energy transfer efficiencies were obtained. The contributions from exciton jumping beyond the nearest neighbor account for 67% of the energy transfer rates for truMOF-1 as shown in Figure 4.

Since the Förster energy transfer rate decreases with increasing donor−acceptor separation in an r^{-6} relationship, the large proportion of longer distance jumping is counterintuitive. Energy transfer over twice the distance will thus be 2^6 or 64 times slower. Our rate calculations in the simulations confirmed such a dependence on distance. One-step jumping over twice the distance takes far more time than two successive hops between nearest neighbors by a factor of 32. One might thus conclude that long distance jumping in energy transfer should be very limited and almost negligible.

However, this argument does not take into account the exponentially increased number of possible paths after adding jumps over longer distances. Although each path has a small contribution to the overall rate, summation over all the possible paths leads to a rate comparable to that of nearest neighbor hopping. We present a simple model net of six molecules in the Supporting Information (Section S7) to illustrate the large contribution of multiple paths in long-distance energy transfer.

Förster Energy Transfer Rate. The traditional Förster resonance energy transfer (FRET) formulation involves a point-dipole model. This point-dipole approximation does not apply at a donor−acceptor separation of less than 2 nm. We thus used a more general Förster equation beyond the point-dipole formulation in our simulation:[40,57−59]

$$k_{tr} = \frac{2\pi}{\hbar} V^2 J \tag{1}$$

where J is the overlap integral between the normalized absorption spectrum of the acceptor and the emission spectra of the donor. V is the exciton coupling between the acceptor and the donor.

The overlap integral, which arises from the energy conservation requirement of the energy transfer, can be obtained from the experimental absorption and emission spectra of the donor and acceptor by

$$J = \frac{\int_0^\infty F_D(\lambda)\varepsilon_A(\lambda)\lambda^4 \, d\lambda}{\hbar c \int_0^\infty F_D(\lambda)\lambda^3 \, d\lambda \int \frac{\varepsilon_A(\lambda)}{\lambda} \, d\lambda} \tag{2}$$

where $F_D(\lambda)$ and $\varepsilon_A(\lambda)$ are the experimental emission spectrum of the donor and absorption spectrum of the acceptor, respectively.

The exciton coupling can be evaluated by columbic coupling between the excited states of the donor and acceptor when wave function overlap between the two is negligible as in the MOF structure. We estimated this columbic coupling using atomic transition densities,[40,57−59] which yields much more reliable results than the point dipole approximation at short ligand−ligand distances.

$$V_{ml} = \frac{1}{4\pi\epsilon_0} \sum_i^{N_m} \sum_j^{N_l} \frac{q_i^t q_j^t}{(R_i^m - R_j^l)} \tag{3}$$

where q_i^t and R_i^m are the atomic transition density and position of the atom i in the molecule m.

These coupling values are different in truMOF-1 and truMOF-2. In truMOF-1, the adjacent ligands in the same tetrahedral cage are very close to each other with interligand coupling of 349 cm^{-1}. The couplings between ligands in different cages are much smaller, with the largest value of 123 cm^{-1}. In truMOF-2, the coupling between closest ligands is only 166 cm^{-1}, a value much smaller than the largest one in truMOF-1, but energy transport in truMOF-2 is more efficient than that in truMOF-1. This is because ligands in truMOF-2 are more connected while ligands in truMOF-1 form more isolated cages. This illustrates the importance of topology in addition to interligand coupling in dictating the efficiency of energy transfer.

The atomic transition densities were obtained from singly excited configuration interaction calculations based on an INDO ground state wave function. The oscillation strength f of the calculated results were normalized to experimental absorption spectra of the donor and acceptor by

$$f = 0.0429 \times \int \frac{\varepsilon(\lambda)}{\lambda^2} \, d\lambda \tag{4}$$

For the **L** ligand with C_{3h} symmetry, there are two degenerate excited states with transition dipole moments in

DOI: 10.1021/jacs.6b01345
J. Am. Chem. Soc. 2016, 138, 5308−5315

the molecular plane. These two degenerate states transform as (x,y) under symmetry operations of the C_{3h} point group and belongs to the E' irreducible representation. The atomic transition density calculations considered the pair of excited states.

The calculated energy transfer rates between adjacent molecules in the crystal structures are very different from those obtained from point-dipole calculations, while the rates between molecules separated by longer distances are very similar for these two methods.

Solving the Model of Exciton Dynamics. Dye molecules were added to the structural model based on calculated adsorption positions and distributions. The number of added dye molecules was kept in accordance with the doping level. The dye adsorption positions were predicted from an annealing calculation with molecular force field using the Adsorber Locater module in Materials Studio software suite, with the first 10 configurations with lowest energies selected. The occupancy probabilities of all dye positions were assigned according to the calculated adsorption energies following the Boltzmann distribution. The final dye molecules in the model were loaded by a machine-generated random number to the configurations with corresponding occupancy probabilities. The calculations were performed for several times with different dye distributions and then averaged to give the final simulation results.

The exciton dynamics was then simulated using the master equations:

$$\frac{\mathrm{d}}{\mathrm{d}t}P_i(t) = P_i(t)\left\{-\frac{1}{\tau_i} - \sum_{j\neq i} k_{i,j}\right\} + \sum_{j\neq i} k_{j,i}P_j(t) \tag{5}$$

or more concisely

$$\frac{\mathrm{d}}{\mathrm{d}t}\vec{P}(t) = \bar{K}\vec{P}(t) \tag{6}$$

where $\vec{P}(t)$ is the column vector describing excitation population at each site including both the ligand molecules and the dye molecules. $\bar{K}$ is the rate matrix that is constructed from the lifetime decay of the excited state on this site $(\frac{1}{\tau_i})$ and energy transfer with all the other sites ($k_{i,j}$ and $k_{j,i}$).

The master equation was solved by propagating the site populations in time

$$\vec{P}(t) = \exp(\bar{K}t)\vec{P}(0) \tag{7}$$

where$\vec{P}(0)$ is the initial excited state populations, being set to unity on all ligand molecules and zero on all dye molecules.

The time-dependent emission intensities of the ligand $I_L(t)$ and the dye $I_D(t)$ can be calculated from the excited state populations by knowing the fluorescence rate Γ, which are determined experimentally from fluorescence lifetime τ and quantum efficiency Φ.

$$\Gamma = \frac{\Phi}{\tau} \tag{8}$$

and

$$I_L(t) = \Gamma_L \cdot P_{\mathrm{ligand}}(t) \tag{9}$$

$$I_D(t) = \alpha \cdot \Gamma_D \cdot P_{\mathrm{dye}}(t) \tag{10}$$

The total emission intensities of the ligand and the dye can be calculated as

$$I_{\mathrm{ligand}} = \int_0^\infty I_L(t)\,\mathrm{d}t \tag{11}$$

$$I_{\mathrm{dye}} = \int_0^\infty I_D(t)\,\mathrm{d}t \tag{12}$$

Diffusivity of Excitons. The diffusivity of the excitons can be evaluated by putting one exciton at the center of the crystalline model, and monitor how this exciton diffuse outward.

Diffusion from a point source in an infinite homogeneous volume can be estimated by

$$P(r,t) = \frac{1}{4\pi Dt}\exp\left(-\frac{r^2}{4Dt}\right) \tag{13}$$

where D is the diffusivity of the exciton.

By fitting the simulations to the above formula, the diffusivities were determined to be 1.8×10^{-2} cm^2/s and 2.3×10^{-2} cm^2/s for truMOF-1 and truMOF-2, respectively. These numbers are relatively large compared to typical values in heterojunction organic solar cells.[15] The exciton migration distances can be estimated by considering a random walk of the exciton in 3D within its lifetime:

$$L = \sqrt{D\tau} \tag{14}$$

The exciton migration distance is calculated to be 43 nm for truMOF-1 and 48 nm for truMOF-2. Importantly, if only considering the nearest neighbor contributions, these migration distances will be reduced to 20 nm in truMOF-1 and 25 nm in truMOF-2. The jumping beyond nearest neighbor thus increases this distance by 115% in truMOF-1 and 92% in truMOF-2.

Jumping Beyond Nearest Neighbor in General Cases. The JBNN can also be significant in other systems besides these truMOFs. To investigate when the JBNN needs to be considered in different energy transport networks, we built a general isotropic model for exciton migration (see SI, Section S8). In this model, we can tune the Förster energy transfer rate constants and monitor the change of the percentage of contributions of JBNN in the overall energy transfer events.

The rate of Förster energy transfer in isotropic media with averaged dipole orientations can be represented by a Förster distance R. When the donor and acceptor are separated by the Förster distance at random orientations, 50% of the donor energy will be transferred to the acceptor. The Förster energy transfer rate is

$$k_F = \frac{1}{\tau_D}\frac{R^6}{r^6} \tag{15}$$

where τ_D is the donor lifetime and r is the donor−acceptor separation.

As an example, the Förster energy transfer distance between the **L** ligands in the truMOFs is 3.5 nm. For comparison, the adjacent ligands in the MOFs are separated by only 0.87−1.8 nm in truMOF-1 and 1.27 nm in truMOF-2. These Förster distances are typical for organic dyes. In photosynthetic antennae in chloroplasts, the Förster distance between chlorophylls is 4.2−9.0 nm,[47,49,60] and the separation between adjacent chlorophylls is 1−1.3 nm,[47−49] which are comparable to the tru-MOFs.

DOI: 10.1021/jacs.6b01345
J. Am. Chem. Soc. 2016, 138, 5308−5315

In the simulation of general isotropic systems, the Förster distances (R_{LL} and R_{LD}) were normalized by the ligand−ligand separation (r_L). For simplification, the ligand-dye distance is set to the same as the ligand−ligand separation in this model. The percentage of contributions from JBNN to I_{ligand}/I_{dye} was evaluated by systematically changing R_{LL}/r_L and R_{LD}/r_L as shown in Figure 7 (see Section S8 in SI for more details).

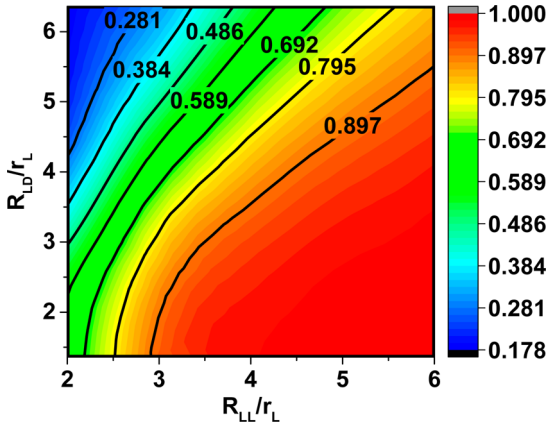

Figure 7. Fraction of JBNN (jump beyond nearest neighbor) in the overall energy transfer rates as a function of normalized Förster distances R_{LL}/r_L (ligand-to-ligand) and R_{LD}/r_L (ligand-to-dye) for dye doping level of 0.5%. The fraction of JBNN is represented by colors on the map with contour lines showing the values.

Contributions of JBNN increase with a faster ligand-to-ligand energy transfer rate (larger R_{LL}/r_L) and decrease with a faster ligand-to-dye energy transfer rate (larger R_{LD}/r_L). This result is rationalized as the long distance jumping mainly affects exciton migration. With a lower ligand-to-dye energy transfer rate, the excitons have more time to migrate on the framework before being transferred to the dye. Similarly, a higher ligand-to-ligand energy transfer rate produces excitons with higher mobility. The contribution of JBNN to the energy transfer is thus affected by both the ligand-to-dye and ligand-to-ligand energy transfer rates, and plays a significant role in a wide range of combinations of these two parameters.

CONCLUSION

We studied the Förster energy transport of singlet excitons in two light-harvesting MOFs built from truxene-based ligands. Both these antenna frameworks efficiently transfer energy to coumarin dye molecules loaded inside the MOF cavity. These systems resemble photosynthetic networks that funnel energy collected by chlorophyll/bacteriochlorophyll arrays to their embedded reaction centers. We found that efficient energy transfer and exciton migration in the MOF system could not be quantitatively explained using the usual step-by-step random hopping model adopted in previous MOF energy transfer analyses. Exciton jumping beyond nearest neighbors was found to account for up to 67% of the energy transfer rates in these systems with singlet excited states. Our work thus presents a significant insight that will shape the design of efficient energy transport networks.

EXPERIMENTAL SECTION

2,7,12-Tribromo-5,5′,10,10′,15,15′-hexaethyltruxene was synthesized according to the literature.[61]

Synthesis of 5,5′,10,10′,15,15′-Hexaethyltruxene-2,7,12-tribenzoate methyl ester (Me_3L). A mixture of 2, 7, 12-tribromo-5,5′,10,10′,15,15′-hexaethyltruxene (408 mg, 0.6 mmol), 4-(methoxycarbonyl)phenylboronic acid (446 mg, 2.4 mmol), Pd[P-(C_6H_5)$_3$]$_4$ (150 mg, 0.13 mmol), K_2CO_3 (1.4 g), THF (20 mL), and H_2O (5 mL) was placed into a 100 mL sealed container with a magnetic stirring bar and evacuated and purged with nitrogen. Then the mixture was heated to 100 °C under nitrogen protection for 3 days. After the mixture was cooled to room temperature, the solvent was removed with a rotary evaporator. The crude product was purified by column chromatography to obtain the pure product (150 mg. 27.3% yield). ^{1}H NMR (400 MHz, $CDCl_3$) δ 8.46 (d, J = 8.1 Hz, 3H), 8.17 (d, J = 8.0 Hz, 6H), 7.82 (d, J = 8.2 Hz, 6H), 7.72 (d, J = 8.4 Hz, 6H), 3.98 (s, 9H), 3.09 (dd, J = 13.8, 7.2 Hz, 6H), 2.27 (dd, J = 13.7, 7.2 Hz, 6H), 0.30 (t, J = 7.1 Hz, 18H).

Synthesis of 5,5′,10,10′,15,15′-Hexaethyltruxene-2,7,12-tribenzoic acid (H_3L). 5, 5′, 10, 10 ′, 15, 15′-hexaethyltruxene-2,7,12-tribenzoate methyl ester (200 mg, 0.36 mmol) was dissolved in a mixture of THF (10 mL), EtOH (10 mL), and 6 M aqueous NaOH solution (10 mL). The mixture was heated to 80 °C and refluxed for 8 h. After the mixture was cooled to room temperature, the organic solvents were removed by a rotary evaptor. The aqueous solution of the solid was adjusted to pH < 1 to precipitate the product which was washed with H_2O several times (180 mg, 94% yield). ^{1}H NMR (400 MHz, DMSO): δ 8.46 (d, J = 8.4 Hz, 3H), 8.09 (d, J = 8.4 Hz, 6H), 7.99 (d, J = 8.5 Hz, 9H), 7.89 (d, J = 7.3 Hz, 3H), 3.02 (dd, J = 13.2, 6.8 Hz, 6H), 2.36 (dd, J = 13.5, 7.0 Hz, 6H), 0.25−0.08 (m, 18H). ^{13}C NMR (126 MHz, DMSO): δ 167.70, 153.66, 144.61, 144.55, 140.34, 138.60, 138.02, 130.49, 129.99, 127.35, 126.26, 125.21,121.23, 57.15, 29.15, 8.94. Elemental analysis: Anal. Calc.: C 82.73%, H 6.25%. Found: C 79%, H 6.3%.)

Synthesis of truMOF-1. A mixture of $Zn(NO_3)_2{\cdot}4H_2O$ (60 mg) and H_3**L** (45 mg) were placed in a mixed solution of DMF (10 mL), CH_3OH (0.3 mL) and H_2O (0.3 mL), with several glass slides in a screw-capped vial, and placed in a 90 °C oven for 2 days. The crystals grew on the glass slides and the slides with crystals were taken out of the solution and thoroughly washed with DMF and EtOH before other experiments.

Synthesis of truMOF-2. A mixture of $Zn(NO_3)_2{\cdot}4H_2O$ (60 mg) and H_3**L** (45 mg) were placed in a mixed solution of DMF (10 mL) and CH_3OH (0.3 mL), with several glass slides in a screw-capped vial, and placed in a 90 °C oven for 2 days. The crystals grew on the glass slides and the slides with crystals were taken out of the solution and thoroughly washed with DMF and EtOH before other experiments.

ASSOCIATED CONTENT

Supporting Information

The Supporting Information is available free of charge on the ACS Publications website at DOI: 10.1021/jacs.6b01345.

Crystal data for truMOF-1 (CIF)
Crystal data for truMOF-2 (CIF)
Ligand Synthesis, Powder X-ray Diffractions, Thermogravimetric Analysis, Fluorescence and UV−vis Spectra, Model Network, Exciton Dynamics Simulation (PDF)

AUTHOR INFORMATION

Corresponding Author

*wangchengxmu@xmu.edu.cn

Present Address

[‖]Key Laboratory of Polyoxometalate Science of the Ministry of Education, Faculty of Chemistry, Northeast Normal University, Changchun, Jilin 130024, PR China.

Author Contributions

[§]Q.Z., C.Z., and L.C. contributed equally.

Notes

The authors declare no competing financial interest.

DOI: 10.1021/jacs.6b01345
J. Am. Chem. Soc. 2016, 138, 5308−5315

■ ACKNOWLEDGMENTS

We thank the National Natural Science Foundation of PR China (21471126), the National Thousand Talents Program of the PR of China (to C.W. and W.L.), and the 985 Program of Chemistry and Chemical Engineering disciplines of Xiamen University for support with funding. Single crystal diffraction studies were performed at ChemMatCARS, APS, Argonne National Laboratory (ANL), which is principally supported by the National Science Foundation (NSF/CHE-1346572). Use of the APS, an Office of Science User Facility operated for the U.S. Department of Energy (DOE) Office of Science by Argonne National Laboratory, was supported by the U.S. DOE under Contract No. DE-AC02-06CH11357. We also thank Prof. Xiaoyu Cao and Mr. Xuefu Hu for help with the ligand synthesis.

■ REFERENCES

(1) Cheng, Y.-C.; Fleming, G. R. *Annu. Rev. Phys. Chem.* **2009**, *60*, 241.
(2) Amerongen, H. v.; Grondelle, R. v.; Valkunas, L. In *Photosynthetic Excitons*; World Scientific, 2011; p 1.
(3) Grover, M.; Silbey, R. *J. Chem. Phys.* **1971**, *54*, 4843.
(4) Van Zandvoort, M.; Wróbel, D.; Lettinga, P.; Ginkel, G. v.; Levine, Y. K. *Photochem. Photobiol.* **1995**, *62*, 279.
(5) Devenney, M.; Worl, L. A.; Gould, S.; Guadalupe, A.; Sullivan, B. P.; Caspar, J. V.; Leasure, R. L.; Gardner, J. R.; Meyer, T. J. *J. Phys. Chem. A* **1997**, *101*, 4535.
(6) Gilat, S. L.; Adronov, A.; Frechet, J. M. J. *Angew. Chem., Int. Ed.* **1999**, *38*, 1422.
(7) Ward, M. D.; Barigelletti, F. *Coord. Chem. Rev.* **2001**, *216−217*, 127.
(8) Odobel, F.; Massiot, D.; Harrison, B. S.; Schanze, K. S. *Langmuir* **2003**, *19*, 30.
(9) Higgins, G. T.; Bergeron, B. V.; Hasselmann, G. M.; Farzad, F.; Meyer, G. J. *J. Phys. Chem. B* **2006**, *110*, 2598.
(10) Thomas, S. W., III; Joly, G. D.; Swager, T. M. *Chem. Rev.* **2007**, *107*, 1339.
(11) Aratani, N.; Kim, D.; Osuka, A. *Acc. Chem. Res.* **2009**, *42*, 1922.
(12) Wasielewski, M. R. *Acc. Chem. Res.* **2009**, *42*, 1910.
(13) Andrew, T. L.; Swager, T. M. *J. Polym. Sci., Part B: Polym. Phys.* **2011**, *49*, 476.
(14) Chen, L.; Furukawa, K.; Gao, J.; Nagai, A.; Nakamura, T.; Dong, Y.; Jiang, D. *J. Am. Chem. Soc.* **2014**, *136*, 9806.
(15) Menke, S. M.; Holmes, R. J. *Energy Environ. Sci.* **2014**, *7*, 499.
(16) Cui, Y.; Yue, Y.; Qian, G.; Chen, B. *Chem. Rev.* **2012**, *112*, 1126.
(17) Zhang, T.; Lin, W. *Chem. Soc. Rev.* **2014**, *43*, 5982.
(18) Hu, Z.; Deibert, B. J.; Li, J. *Chem. Soc. Rev.* **2014**, *43*, 5815.
(19) So, M. C.; Wiederrecht, G. P.; Mondloch, J. E.; Hupp, J. T.; Farha, O. K. *Chem. Commun.* **2015**, *51*, 3501.
(20) Zhang, X.; Wang, W.; Hu, Z.; Wang, G.; Uvdal, K. *Coord. Chem. Rev.* **2015**, *284*, 206.
(21) O'Keeffe, M.; Eddaoudi, M.; Li, H. L.; Reineke, T.; Yaghi, O. M. *J. Solid State Chem.* **2000**, *152*, 3.
(22) Ferey, G.; Mellot-Draznieks, C.; Serre, C.; Millange, F. *Acc. Chem. Res.* **2005**, *38*, 217.
(23) Inokuma, Y.; Kawano, M.; Fujita, M. *Nat. Chem.* **2011**, *3*, 349.
(24) Herm, Z. R.; Wiers, B. M.; Mason, J. A.; van Baten, J. M.; Hudson, M. R.; Zajdel, P.; Brown, C. M.; Masciocchi, N.; Krishna, R.; Long, J. R. *Science* **2013**, *340*, 960.
(25) Shustova, N. B.; McCarthy, B. D.; Dincă, M. *J. Am. Chem. Soc.* **2011**, *133*, 20126.
(26) An, J.; Shade, C. M.; Chengelis-Czegan, D. A.; Petoud, S.; Rosi, N. L. *J. Am. Chem. Soc.* **2011**, *133*, 1220.
(27) Liu, Y.; Pan, M.; Yang, Q.-Y.; Fu, L.; Li, K.; Wei, S.-C.; Su, C.-Y. *Chem. Mater.* **2012**, *24*, 1954.
(28) Williams, D. E.; Rietman, J. A.; Maier, J. M.; Tan, R.; Greytak, A. B.; Smith, M. D.; Krause, J. A.; Shustova, N. B. *J. Am. Chem. Soc.* **2014**, *136*, 11886.
(29) Yu, J.; Cui, Y.; Xu, H.; Yang, Y.; Wang, Z.; Chen, B.; Qian, G. *Nat. Commun.* **2013**, DOI: 10.1038/ncomms3719.
(30) Cui, Y.; Song, R.; Yu, J.; Liu, M.; Wang, Z.; Wu, C.; Yang, Y.; Wang, Z.; Chen, B.; Qian, G. *Adv. Mater.* **2015**, *27*, 1420.
(31) Dong, M.-J.; Zhao, M.; Ou, S.; Zou, C.; Wu, C.-D. *Angew. Chem., Int. Ed.* **2014**, *53*, 1575.
(32) Park, J.; Feng, D.; Yuan, S.; Zhou, H.-C. *Angew. Chem., Int. Ed.* **2015**, *54*, 430.
(33) Yanai, N.; Kitayama, K.; Hijikata, Y.; Sato, H.; Matsuda, R.; Kubota, Y.; Takata, M.; Mizuno, M.; Uemura, T.; Kitagawa, S. *Nat. Mater.* **2011**, *10*, 787.
(34) Lan, A.; Li, K.; Wu, H.; Olson, D. H.; Emge, T. J.; Ki, W.; Hong, M.; Li, J. *Angew. Chem., Int. Ed.* **2009**, *48*, 2334.
(35) Foster, M. E.; Azoulay, J. D.; Wong, B. M.; Allendorf, M. D. *Chem. Sci.* **2014**, *5*, 2081.
(36) Zhang, X.; Ballem, M. A.; Hu, Z.-J.; Bergman, P.; Uvdal, K. *Angew. Chem., Int. Ed.* **2011**, *50*, 5729.
(37) Kent, C. A.; Mehl, B. P.; Ma, L.; Papanikolas, J. M.; Meyer, T. J.; Lin, W. *J. Am. Chem. Soc.* **2010**, *132*, 12767.
(38) Kent, C. A.; Liu, D.; Ma, L.; Papanikolas, J. M.; Meyer, T. J.; Lin, W. *J. Am. Chem. Soc.* **2011**, *133*, 12940.
(39) Lee, C. Y.; Farha, O. K.; Hong, B. J.; Sarjeant, A. A.; Nguyen, S. B. T.; Hupp, J. T. *J. Am. Chem. Soc.* **2011**, *133*, 15858.
(40) Son, H. J.; Jin, S.; Patwardhan, S.; Wezenberg, S. J.; Jeong, N. C.; So, M.; Wilmer, C. E.; Sarjeant, A. A.; Schatz, G. C.; Snurr, R. Q.; Farha, O. K.; Wiederrecht, G. P.; Hupp, J. T. *J. Am. Chem. Soc.* **2013**, *135*, 862.
(41) Kent, C. A.; Liu, D.; Ito, A.; Zhang, T.; Brennaman, M. K.; Meyer, T. J.; Lin, W. *J. Mater. Chem. A* **2013**, *1*, 14982.
(42) So, M. C.; Jin, S.; Son, H.-J.; Wiederrecht, G. P.; Farha, O. K.; Hupp, J. T. *J. Am. Chem. Soc.* **2013**, *135*, 15698.
(43) Jin, S.; Son, H.-J.; Farha, O. K.; Wiederrecht, G. P.; Hupp, J. T. *J. Am. Chem. Soc.* **2013**, *135*, 955.
(44) Lin, J.; Hu, X.; Zhang, P.; Van Rynbach, A.; Beratan, D. N.; Kent, C. A.; Mehl, B. P.; Papanikolas, J. M.; Meyer, T. J.; Lin, W.; Skourtis, S. S.; Constantinou, M. *J. Phys. Chem. C* **2013**, *117*, 22250.
(45) Maza, W. A.; Ahrenholtz, S. R.; Epley, C. C.; Day, C. S.; Morris, A. J. *J. Phys. Chem. C* **2014**, *118*, 14200.
(46) Maza, W. A.; Padilla, R.; Morris, A. J. *J. Am. Chem. Soc.* **2015**, *137*, 8161.
(47) Byrdin, M.; Jordan, P.; Krauss, N.; Fromme, P.; Stehlik, D.; Schlodder, E. *Biophys. J.* **2002**, *83*, 433.
(48) Liu, Z.; Yan, H.; Wang, K.; Kuang, T.; Zhang, J.; Gui, L.; An, X.; Chang, W. *Nature* **2004**, *428*, 287.
(49) Pålsson, L. O.; Spangfort, M. D.; Gulbinas, V.; Gillbro, T. *FEBS Lett.* **1994**, *339*, 134.
(50) Renger, T.; May, V.; Kuhn, O. *Phys. Rep.* **2001**, *343*, 137.
(51) Tamiaki, H.; Shibata, R.; Mizoguchi, T. *Photochem. Photobiol.* **2007**, *83*, 152.
(52) Kent, C. A.; Liu, D.; Meyer, T. J.; Lin, W. *J. Am. Chem. Soc.* **2012**, *134*, 3991.
(53) Murata, N.; Araki, S.; Fujita, Y.; Suzuki, K.; Kuwabara, T.; Mathis, P. *Photosynth. Res.* **1986**, *9*, 63.
(54) Noy, D.; Moser, C. C.; Dutton, P. L. *Biochim. Biophys. Acta, Bioenerg.* **2006**, *1757*, 90.
(55) van Grondelle, R. *Biochim. Biophys. Acta, Rev. Bioenerg.* **1985**, *811*, 147.
(56) The ligand in MOF structure has absorption maximum at 370 nm, while free acid ligand has absorption maximum at 333 nm.
(57) Wong, K. F.; Bagchi, B.; Rossky, P. J. *J. Phys. Chem. A* **2004**, *108*, 5752.
(58) Howard, I. A.; Zutterman, F.; Deroover, G.; Lamoen, D.; Van Alsenoy, C. *J. Phys. Chem. B* **2004**, *108*, 19155.
(59) Patwardhan, S.; Sengupta, S.; Würthner, F.; Siebbeles, L. D. A.; Grozema, F. *J. Phys. Chem. C* **2010**, *114*, 20834.

DOI: 10.1021/jacs.6b01345
J. Am. Chem. Soc. 2016, 138, 5308−5315

(60) Şener, M.; Strümpfer, J.; Hsin, J.; Chandler, D.; Scheuring, S.; Hunter, C. N.; Schulten, K. *ChemPhysChem* **2011**, *12*, 518.
(61) Yuan, M.-S.; Wang, D.-E.; Li, T.-B.; Xu, Y.; Wang, W.-J.; Tu, Q.; Zhang, Y.; Li, M.; Wang, J. *Dyes Pigm.* **2014**, *107*, 60.

DOI: 10.1021/jacs.6b01345
J. Am. Chem. Soc. 2016, 138, 5308−5315